RESEARCH ARTICLE

METALLURGY

Kink bands promote exceptional fracture resistance in a NbTaTiHf refractory medium-entropy alloy

David H. Cook^{1,2}†, Punit Kumar²†*, Madelyn I. Payne^{1,2}, Calvin H. Belcher³, Pedro Borges^{1,2}, Wenqing Wang^{1,2}, Flynn Walsh^{1,2}, Zehao Li⁴, Arun Devaraj⁴, Mingwei Zhang^{2,5}‡, Mark Asta^{1,2}, Andrew M. Minor^{1,2,5}, Enrique J. Lavernia³§, Diran Apelian³, Robert O. Ritchie^{1,2}*

Single-phase body-centered cubic (bcc) refractory medium- or high-entropy alloys can retain compressive strength at elevated temperatures but suffer from extremely low tensile ductility and fracture toughness. We examined the strength and fracture toughness of a bcc refractory alloy, NbTaTiHf, from 77 to 1473 kelvin. This alloy's behavior differed from that of comparable systems by having fracture toughness over 253 MPa·m $^{1/2}$, which we attribute to a dynamic competition between screw and edge dislocations in controlling the plasticity at a crack tip. Whereas the glide and intersection of screw and mixed dislocations promotes strain hardening controlling uniform deformation, the coordinated slip of <111> edge dislocations with {110} and {112} glide planes prolongs nonuniform strain through formation of kink bands. These bands suppress strain hardening by reorienting microscale bands of the crystal along directions of higher resolved shear stress and continually nucleate to accommodate localized strain and distribute damage away from a crack tip.

etallic structural materials tend to have a trade-off between strength and toughness (1). This problem is most apparent in materials intended for extreme environments, particularly at high temperatures. In the past half century, the urgent need to reduce carbon emissions by increasing fuel efficiency has motivated the development of materials intending to surpass the hightemperature performance of superallovs, such as Si-containing refractories and TiAl (2, 3). These materials have been designed to have high strength at high temperatures; however, engineering them to concurrently possess damage tolerance, particularly at low temperatures where many of these materials are below their ductile-to-brittle transition temperatures, is difficult and has disqualified nearly all of them from safety-critical applications (4, 5).

Single-phase bcc refractory high- or mediumentropy alloys (RHEAs or RMEAs) composed of high concentrations of Group IV, V, and VI

elements have been identified as an attractive design space for high-temperature materials (6). Unfortunately, RHEAs have large strengthtoughness trade-offs. Although some of these alloys, particularly the group V and VI mixtures such as NbMoTaW and its derivatives, possess impressive compressive strengths at temperatures up to 1900 K (7, 8), they suffer from extremely low fracture toughness and tensile ductility at all temperatures (9). On the opposite end of this spectrum, the group IV and V mixtures, particularly the model HfNbTaTiZr alloy, can exhibit substantial tensile plasticity and even high ambient temperature fracture toughness (10). However, these systems do not possess adequate thermodynamic phase stability, which is detrimental to their high-temperature mechanical properties (11-14).

Theories for the high-temperature strength of these systems are based on the reduced mobility of edge dislocations and the pinning of screw dislocations by atomic jogs (15-18). However, no clear understanding exists for the high room-temperature toughness of 211 MPa·m^{1/2} reported for the HfNbTaTiZr alloy (10). Tensile tests of this material only add further mystery because the alloy exhibits low uniform tensile ductility (~4%) and a marked absence of strain hardening, which, unlike the face-centered cubic (fcc) high-entropy alloys (19), indicates that the toughness should be very low (20). Analysis of the room-temperature deformation structures reveals that, although bulk plastic flow is controlled by the lethargic motion of screw-character dislocations, local ductility can nonetheless be accommodated by collective arrays of edge dislocations, which form pairs of tilt boundaries known as kink bands (20, 21). As described in zinc (22), the formation of tl bands reorients crystalline slip planes along directions of high resolved shear stress, softening the material (23-25). In polycrystalline materials, kink bands nucleate in regions of high dislocation density and propagate across grains to relax the associated stress concentration (26). Their formation in RHEAs with a high concentration of group IV elements (20, 21). as well as in pure group V bcc elements (27), should be detrimental to the toughness, as this mechanism in tension promotes plastic instability by suppressing uniform ductility and is thus associated with the onset of fracture. We demonstrate that in a specifically engineered alloy, kink bands can induce a remarkable response as an exceptionally potent intrinsic toughening mechanism that does not necessarily inhibit high-temperature strength.

Results and discussion

Specifically, we investigated the mechanical properties of a nonequiatomic Nb₄₅Ta₂₅Ti₁₅Hf₁₅ RMEA from 77 to 1473 K by performing uniaxial tensile tests and nonlinear elastic J-integralbased fracture toughness tests. The material was designed by alloying group IV elements (Ti and Hf) with group V elements (Nb and Ta) to (i) ductilize the material, (ii) generate lattice distortion to allow for high-temperature strength retention, and most notably, (iii) to prioritize high-temperature bcc thermodynamic stability lacking in RHEAs containing Zr and with higher concentations of group IV elements (28, 29). More information on the details of the alloy design can be found in (30). To make the material chemically and microstructurally homogeneous, we arc-melted high-purity elemental ingots several times and rolled them at room temperature to reduce the thickness by ~33% then heat treated at 1373 K for one hour and water quenched. This process produced a near fully recrystallized, single-phase microstructure with equiaxed grains of an average size of 270 µm and some smaller partially recrystallized grains of a diameter of ~20 µm (Fig. 1B and fig. S1). X-ray diffraction (XRD) (Fig. 1C) confirmed that the material formed a single bcc phase with the exact composition measured by inductively coupled plasma atomic emission spectroscopy of 43.98 atomic % (at %) Nb, 24.21 at % Ta, 14.77 at % Ti, and 14.75 at % Hf. We listed the remaining trace elements introduced during arc-melting in table S1. We measured C and N interstitial elements by combustion to be 0.059 and 0.0495 at % (60 and 58 ppm), respectively. We measured an O concentration of 0.146 at % (197 ppm) by inert gas fusion. This brought the total interstitial content to ~0.25 at % (315 ppm). To understand the distribution of interstitial elements, we used atom probe tomography to further investigate the material, (fig. S2) which revealed no

†These authors contributed equally to this work. ‡Present address: Department of Materials Science and Engineering, University of California, Davis, CA, USA.

§Present address: Department of Materials Science and Engineering, Department of Mechanical Engineering, Texas A&M University, College Station, TX, USA.

Cook et al., Science 384, 178–184 (2024) 12 April 2024

¹Department of Materials Science and Engineering, University of California, Berkeley, CA, USA. ²Materials Sciences Division, Lawrence Berkeley National Laboratory, Berkeley, CA, USA. ³Department of Materials Science and Engineering, University of California, Irvine, CA, USA. ⁴Physical and Computational Sciences Directorate, Pacific Northwest National Laboratory, Richland, WA, USA. ⁵National Center for Electron Microscopy, Molecular Foundry, Lawrence Berkeley National Laboratory, Berkeley, CA, USA.

^{*}Corresponding author. Email: kpunit@berkeley.edu (P.K.); roritchie@lbl.gov (R.O.R.)

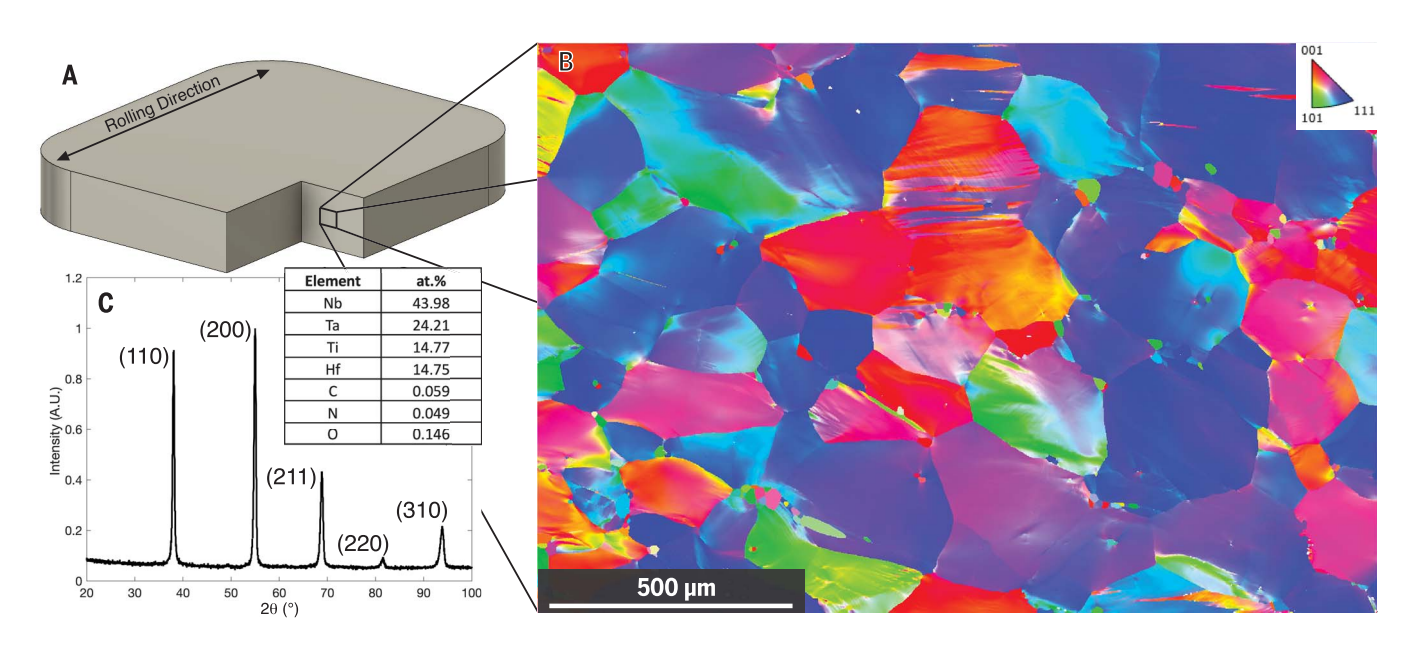


Fig. 1. Initial microstructure of Nb₄₅**Ta**₂₅**Ti**₁₅**Hf**₁₅**.** (**A**) To produce the alloy, high-purity elements were arc-melted, forged, and cold rolled to a reduction in thickness of ~33%, annealed at 1373 K for one hour, and water quenched. This process produced the microstructure in (**B**), near-fully recrystallized grains of an average diameter of 270 μm. (**C**) XRD confirms the single bcc phase structure. The total interstitial content of the material is ~0.25 at % C, N, and O. A.U., arbitrary units.

segregation of interstitials throughout the matrix and grain boundaries.

We performed uniaxial tensile tests, plotted as engineering stress versus strain (Fig. 2C), at five temperatures: 77 K (liquid nitrogen), 298 K (room temperature), 1073 K, 1223 K, and 1473 K. At room temperature, the alloy exhibited a yield strength (σ_v) of 596 MPa and a uniform ductility of 15.5%. As the temperature was lowered into the cryogenic regime, the strength increased to 937 MPa, and the uniform ductility experienced a modest decrease from room temperature to 9%. Conversely, as the temperature was increased through 1073 and 1223 K, the alloy's yield strength gradually decreased by, respectively, ~36% (380 MPa at 1073 K) and ~43% (341 MPa at 1223 K) compared with room temperature. At these temperatures, the uniform ductility also decreased to 2.3% and 1.1%. At 1473 K, a more rapid drop-off in yield strength of ~76% (140 MPa) occurred, and the uniform ductility slightly increased to 2%. Analysis of the strain-hardening behavior in fig. S3 revealed a trend that runs counter to most materials, specifically that the strain hardening increased with increasing temperature. At 77 K, the strain-hardening exponent n was 0.09; as the temperature was increased to room temperature, the material exhibited two-stage hardening (31), with the second strain-hardening exponent increasing to n_2 = 0.14. At higher temperatures, it generally continued to increase: 0.21 at 1073 K, 0.05 at 1223 K, and 0.33 at 1473 K.

To measure the fracture toughness, we evaluated the crack-resistance curves (R curves) with the nonlinear elastic energy release rate, the Jintegral (kJ/m^2) , as a function of the crack ex-

tension, Δa . Unlike most RHEAs, Nb₄₅Ta₂₅Ti₁₅Hf₁₅ exhibited stable crack growth and markedly rising R curve behavior at all temperatures (Fig. 2, A and B). To measure a valid, size-independent fracture toughness value (J_{Ic}), samples must satisfy the J dominance criteria in plane strain, i.e., that the uncracked ligament (b) and thickness (B) > $10(J_{\rm Q}/\sigma_{\rm f})$, where $J_{\rm Q}$ is the conditional toughness calculated by the intersection of the blunting line with the R curve, and σ_f is the flow stress (the average of the yield and maximum tensile stresses). This condition was met for samples at 77, 1073, and 1223 K but not at room temperature or 1473 K. Instead of this, a minimum bound fracture toughness (J_{Icmin}) can be calculated by rearranging the above equation to $J_{\rm Ic,min}$ = $B\sigma_{\rm f}/10$, which, combined with $J_{\rm Q}$, gives a range for the true value. Thus, at room temperature, the fracture toughness (in terms of the stress intensity) lay in the range of 253 MPa·m^{1/2} < K_{JIc} < 323 MPa·m^{1/2}. When the temperature was lowered into the cryogenic regime, the crack-initiation toughness remained persistently high at ~86 MPa·m^{1/2} and rose to a steady-state crack-growth toughness of $K_{\rm ss} \sim 146~{\rm MPa \cdot m^{1/2}}$. At elevated temperatures, the material also continued to exhibit rising R curve behavior. At 1073 K, K_{JIc} was ~67 MPa·m^{1/2}, which rose to a steady-state value of K_{ss} ~93 MPa·m^{1/2}. At 1223 K, the crackinitiation and steady-state fracture toughness decreased to ~52 and ~66 MPa·m^{1/2}, respectively. At 1473 K, the crack-initiation toughness increased again and was in the range 68 MPa·m^{1/2} $< K_{IIc} < 88 \text{ MPa·m}^{1/2}$. These values were all high and unusual; they were indeed remarkable for

Refractory bcc alloys (dilute and concentrated solid solutions) typically exhibit low roomtemperature fracture toughness, which has severely limited their safety-critical engineering applications (4, 32–35). To put $Nb_{45}Ta_{25}Ti_{15}Hf_{15}$ in perspective, NbMoTaW has a room-temperature fracture toughness of 0.2 to 2 MPa·m^{1/2}, which is over two to three magnitudes lower than the minimum room-temperature $K_{\rm Jlc}$ of 253 MPa·m $^{1/2}$ obtained for Nb₄₅Ta₂₅Ti₁₅Hf₁₅ (4). Even traditional refractory alloys based on Nb with tensile ductility do not have low temperature fracture toughness of more than ~40 MPa·m1/2 (36). Strategies to improve the fracture toughness of refractories have historically involved alloying high concentrations of Re (an expensive and rare element) into W, which improves the fracture toughness up to 60 MPa·m^{1/2}, but these alloys do not exhibit rising R curve behavior (37). To understand the reason for this material's extraordinary resistance to fracture, especially over a very wide range of temperatures from 77 to 1473 K, we first investigated the crack-tip deformation mechanisms across all temperatures with postfracture electron backscatter diffraction (EBSD) analysis.

To investigate the deformation mechanisms, the compact-tension C(T) specimens that we used in the fracture toughness tests were cut through the midthickness ($\sim B/2$) perpendicular to the crack to sample the region that experiences the highest stress triaxiality, i.e., the region under complete or near-complete plane-strain conditions. We ground samples and polished them for examination with EBSD to understand the crystallographic changes induced by a propagating crack.

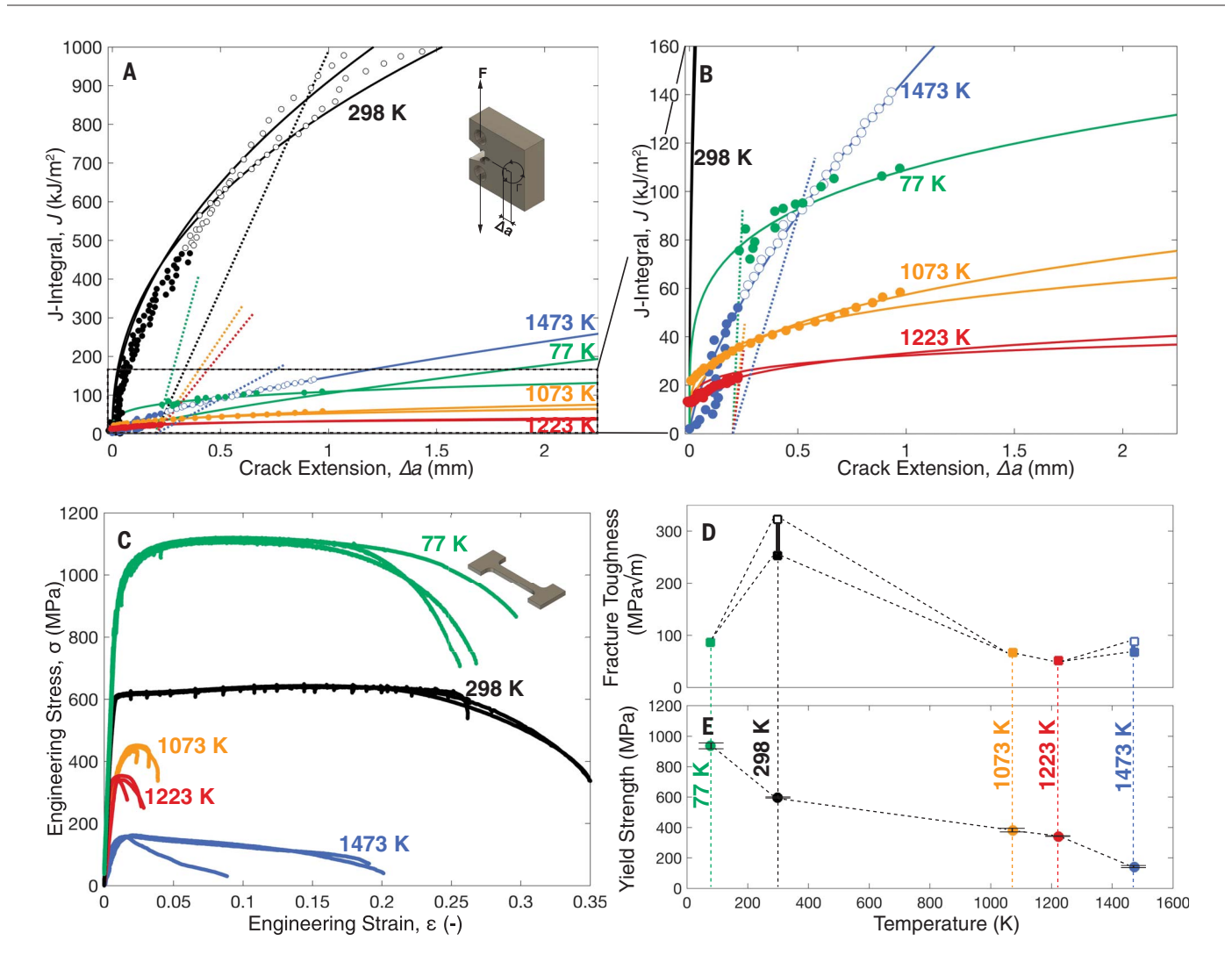


Fig. 2. Mechanical properties of Nb₄₅**Ta**₂₅**Ti**₁₅**Hf**₁₅**.** (**A**) J-integral R curves as a function of crack extension at 77, 298, 1073, 1223, and 1473 K and (**B**) a closer view of R curves measured at extreme temperatures. (**C**) Tensile engineering stress-strain curves measured from 77 to 1473 K. The dynamic strain aging at 298 K corresponds to formation of Lüders bands, whereas the stress drops at 77 K correspond to twinning, which was accompanied by acoustic emission. (**D**) Fracture toughness (K_{Jlc}) calculated from J_{Ic} values obtained from the R curves and (**E**) yield strength (σ_{y}) as a function of temperature. Error bars represent the standard deviation of the yield strength; however, some are smaller

than the data symbols and are therefore not visible. Note that in (D), the $\rm Nb_{45}Ta_{25}Ti_{15}Hf_{15}$ alloy not only retains strength at high temperatures but also exhibits extraordinary fracture toughness at all temperatures: 86 MPa·m $^{1/2}$, 253 to 323 MPa·m $^{1/2}$, 67 MPa·m $^{1/2}$, 52 MPa·m $^{1/2}$, and 68 to 88 MPa·m $^{1/2}$ at the five temperatures from 77 to 1473 K, respectively. The room-temperature fracture toughness is the highest of any known single-phase bcc material, and even higher than fcc CrCoNi-based HEAs (19). Open circles in (A), (B), and (D) denote values that are not strictly valid; the second liquid nitrogen test was excluded from (B) for a clear visualization.

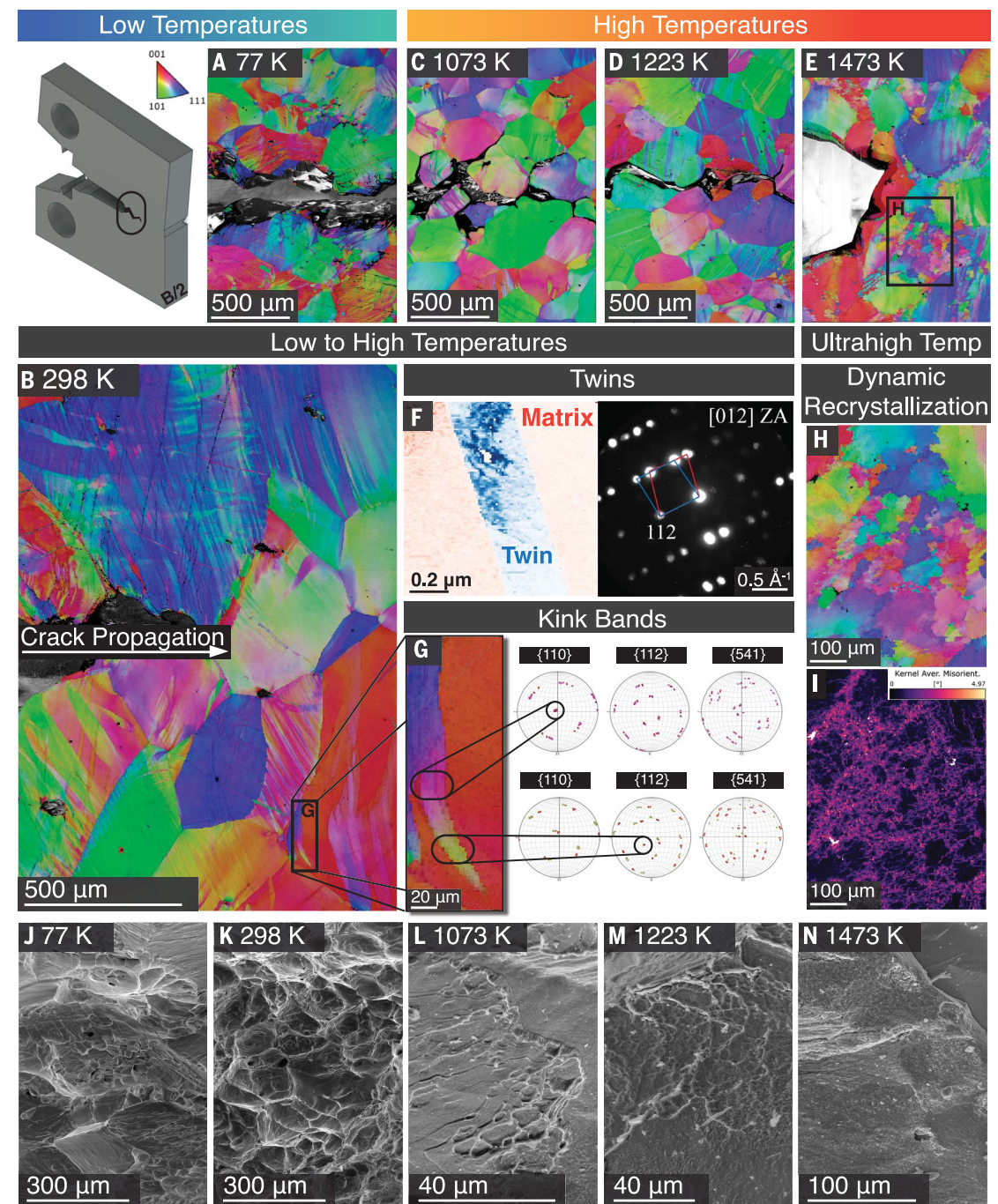
EBSD band contrast (BC) and inverse pole figure (IPF) maps (Fig. 3, A to E) showed the temperature-dependent evolution of deformation mechanisms. At room temperature (Fig. 3B), we observed conventional dislocation glide, {112}<111> twinning (Fig. 3F), and deformation kink bands accommodating the deformation. These rather unusual kink bands are the prominent mechanism, which we discovered in the kernel average misorientation map (fig. S4). These observations indicated that most of the geometrically necessary dislocations are confined to their boundaries. Although most boundaries of these kink bands formed low misorientations (~2° to 8°)

with respect to the matrix of their parent grains, some were as high as 40°. In the cryogenic regime, the salient mechanisms did not change, but their relative ratio did (Fig. 3A). Dislocation motion was still present (Fig. 3F), but {112}<111> twins became more predominant and coarser (up to ~11-µm thick). Although deformation kink bands continued to form, there were fewer of them. Fracture surfaces at room temperature (Fig. 3L) showed ductile microvoids with approximately 100- to 300-µm diameters. In the cryogenic regime, the microvoids decreased in size to ~35 µm, and cleavage facets appeared that were absent in the tensile tests at this temperature (fig. S5A)

owing to the stress triaxiality present in precracked C(T) samples.

At higher temperatures (1073 and 1223 K) (Fig. 3, C to D), the mechanisms stayed nominally the same. Conventional dislocation motion was still observed, kink bands formed, and {112} <111> twinning occurred, the last of which is noteable for bcc materials at elevated temperatures (38). Another feature at these temperatures is that fracture occurs along grain boundaries. Nevertheless, we observed microvoids on the fracture surfaces (Figs. 3, M to N), indicating that substantial plastic deformation can occur before the onset of crack growth. As the crack followed the intergranular path, it branched

Fig. 3. Deformation mechanisms and fracture morphology of Nb₄₅Ta₂₅Ti₁₅Hf₁₅ from 77 to 1473 K. (A to E) EBSD BC and IPF maps of the fracture path (from left to right). Samples were taken at the midthickness of the C(T) samples to investigate mechanisms present in the region of highest stress triaxiality. Deformation twinning was identified by EBSD at temperatures from cryogenic (77 K) to 1223 K. (F) 4D-STEM image of a {112}<111> twin in the wake of the fracture path at 77 K. (G) A kink band in the plastic zone directly ahead of the crack at 298 K and associated intragranular misorientation axis analysis shows that this kink band twists internally from kinking a plane in the {112} family to kinking a plane in the {110} family. (F) At ultrahigh temperatures (1473 K), these mechanisms are replaced by dynamic recrystallization shown in (H) and (I), which destroys the original grain boundaries, inhibiting the mechanism that promotes intergranular fracture. (J to M) Fracture surfaces show a mixture of cleavage and ductile microvoid coalescence at 77 K (J), microvoid coalescence at 298 K (K), and mixed intergranular fracture and microvoid coalescence at 1073 and 1223 K ((L) and (M)]. The fracture surfaces are destroyed by oxidation at 1473 K (N).



substantially. This branching led the crack away from the mode I plane until it was subsequently arrested owing to a lack of a driving force, an additional extrinsic toughening mechanism (I). At 1473 K these mechanisms were supplanted by the diffusion-mediated nucleation of new, more favorably oriented grains, which substantially blunted the crack tip and prevented crack growth (Fig. 3, E, H, and I). At this temperature, we observed bands in most grains. However, their boundaries were altered by the recrystallization processes, such that they cannot be easily identified as kink bands.

12 April 2024

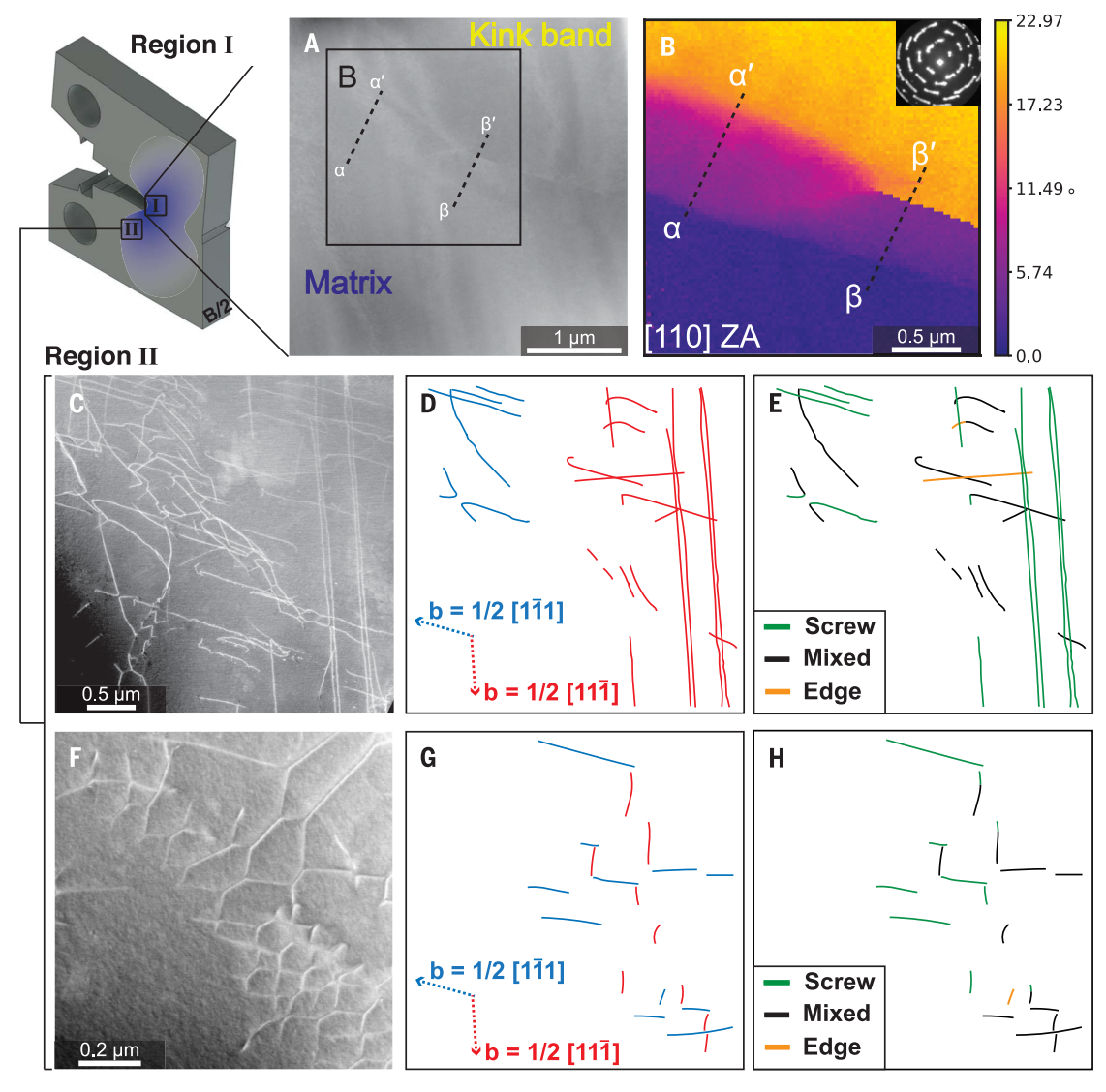
Cook et al., Science 384, 178-184 (2024)

Consistent with prior reports on Group IV-rich RHEAs in tension and compression, EBSD maps (Fig. 3) showed profuse deformation kink bands (20, 21, 39–42). However, the role played by kink bands on the overall behavior in the presence of a sharp crack is not established. To understand how kinking elevates toughness, particularly at lower temperatures at which the toughness of bcc materials suffers, we first performed an intragranular misorientation axis analysis to identify the crystallographic planes active in kink band formation (43). Because a kink band is a tilt boundary formed by locali-

zation of edge-character dislocations, the type of dislocations that form them can be identified if the possible active slip systems and the kink band rotation (Taylor) axis are known (43). This analysis (Fig. 3G and figs. S6 to S11) showed that all the identified kink bands are formed predominantly by $a_0/2<111>\{112\}$ edge dislocations, with the rest formed by $a_0/2<111>\{110\}$ edge dislocations (more often at higher temperatures). This indicates that multiple slip systems are active in kink band formation. Figure 3G even shows that a single kink band can be a result of bending of a $\{112\}$ and a $\{110\}$ lattice

4 of 7

Fig. 4. Kink band and lattice dislocations. Two regions from the C(T) sample tested at 298 K were investigated by TEM: region I corresponds to (A) and (B) and is from a kink band boundary close to the crack tip where plastic strains are high, whereas region II corresponds to insets (C to H) and shows the dislocations present in the matrix in the wake of the crack where plastic strains are lower. (A) High-angle annular darkfield (HAADF) overview image of the focused ion beam lift-out sample. (B) Rotation map from 4D-STEM dataset. (Inset) An aggregate diffraction pattern from all pixels that indicates the rotation of the lattice. [(C) and (F)] HAADF overview of dislocations of screw, edge, and mixed character. [(D) and (G)] Schematics of dislocations colored by their respective Burgers vector: red line, $^{1}/_{2}[11\bar{1}]$; blue line, $^{1}/_{2}[1\bar{1}1]$. The Burgers vector directions are annotated in the figure. [(E) and (H)] Schematics of the same dislocations colored by their character.



plane along different lengths. The tortuous form of this kink band indicates that if kinking is no longer favored by one slip system, another slip system can activate to extend the kink band. Coupled with our observations that kink bands can vary in width and length (not necessarily traversing entire grains), intersect, and nucleate within each other (Fig. 3, A to D), this demonstrates that the versatility of this mechanism enables it to accommodate exceptionally high strains at a crack tip that conventional, uncoordinated dislocation glide and twinning simply cannot.

To further understand their nanoscale structure, we analyzed a small section of a {112} kink band near the room-temperature crack tip using scanning nanobeam diffraction, also known as four-dimensional scanning transmission electron microscopy (4D-STEM). The

resulting images elucidated several features (Fig. 4, A and B). First, we confirmed that kink bands are pure tilt boundaries, evidenced by the rotation of the diffraction pattern about the [110] zone axis (Fig. 4B), which necessitates the presence of pure $a_0/2<111>\{112\}$ edge dislocations. Second, the rotation across the boundary (θ) is not always perfectly discrete, where the points α - α' show a gradient in orientation in contrast to β - β' , which suggests that along certain lengths of the boundary, edge dislocations cannot perfectly space themselves without temperature-activated, nonconservative motion. Third, the spacing between dislocations necessary to produced the measured misorientation across the boundary was calculated using the Read-Shockley equation, $d \approx b/\sin\theta$ (44), which revealed that the distance between edge dislocation cores (d) is 7.4 Å apart on this boundary, making the individual dislocations too close to resolve with diffraction contrast TEM.

The prevalence of kink bands indicates that edge dislocation glide is highly active on the $a_0/2 < 111 > \{110\}$ and $\{112\}$ slip systems. However, kink bands do not solely account for the crack-tip plasticity. To gain a holistic picture of the deformation mechanisms, we focused on the edge of the plastic zone in the roomtemperature C(T) samples to (i) study the dislocations responsible for the uniform plastic deformation that occurs at lower strains during the first stages of crack-tip plasticity and (ii) to distinguish the dislocations responsible for kink band formation from those responsible for the uniform plastic deformation. To identify the dislocations, we performed a $\vec{g} \cdot \vec{b}$ analysis. We show dislocations with Burgers

5 of 7

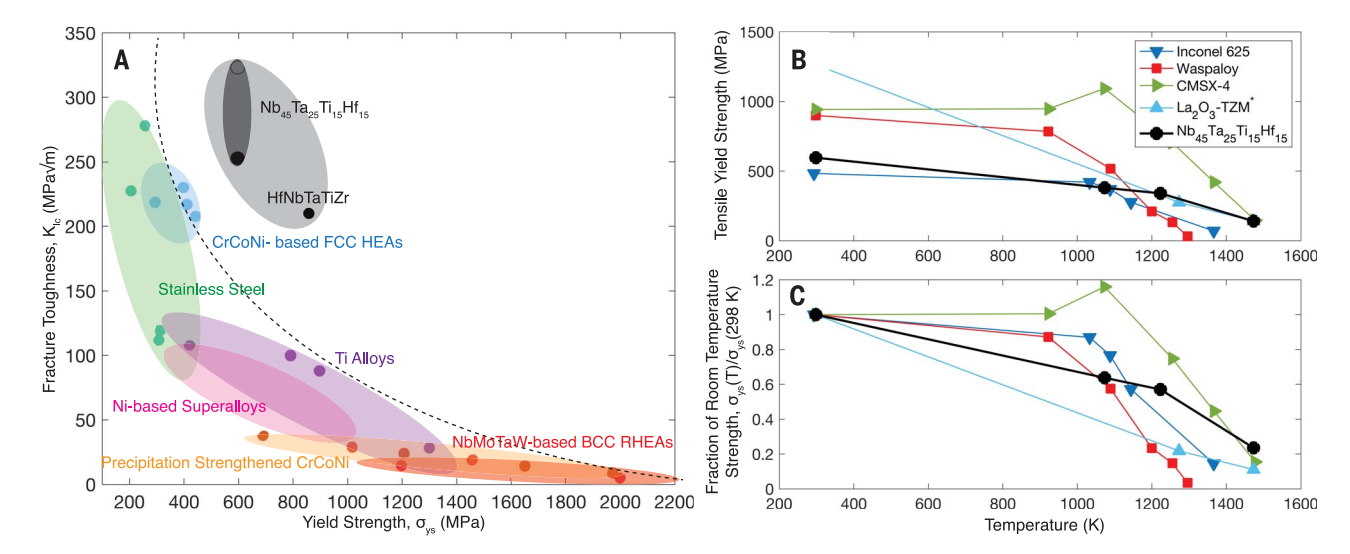


Fig. 5. The Nb $_{45}$ **Ta** $_{25}$ **Ti** $_{15}$ **Hf** $_{15}$ **RHEA in comparison to other structural materials.** (**A**) Room-temperature fracture toughness versus yield strength "banana plot" of Nb $_{45}$ Ta $_{25}$ Ti $_{15}$ Hf $_{15}$ as well as other high-entropy alloys and commercial materials (4, 9, 10, 34, 48, 57–59). This RHEA has an exceptional balance of strength and toughness across a broad range of temperatures (60–63). (**B**) Yield strength versus temperature plots show that Nb $_{45}$ Ta $_{25}$ Ti $_{15}$ Hf $_{15}$

outcompetes most commercial grade high-temperature materials above intermediate temperatures, and (\mathbf{C}) shows that, despite its relatively low room-temperature tensile yield strength, it has exceptional tensile strength retention at 1473 K, surpassing even the Ni-base superalloy CMSX-4 beyond 1400 K. The mechanical properties of titanium-zirconium-molybdenum (TZM) were obtained in vacuo.

vectors $a_0/2[1\bar{1}1]$ and $a_0/2[11\bar{1}]$ in Fig. 4, C to H. Unlike the kink bands that were formed by $a_0/2 < 111 > \{110\}$ or $\{112\}$ edge dislocations. the dislocations in the matrix are a mixture of long straight screw dislocations in addition to mixed and some edge. The presence of mixed and edge character dislocations (though there were few of the latter) suggests that their mobility is decreased in comparison to screw dislocations. Although edge (and mixed) dislocations are rarely observed in elemental bcc metals and dilute alloys owing to their very high mobility, they have been observed in RHEAs and theorized to explain the high-temperature strength of these materials (16, 45). Taken together with the observation of kink bands closer to the crack tip, a qualitative sequence of mechanisms emerged. Whereas the plasticity at the crack tip is initially controlled by the glide of screw and mixed dislocations, ultimately, the coordinated glide of edge dislocations at higher strains results in kinking of the {110} and {112} planes (26). Although the screw and mixed dislocations interact with themselves. grain boundaries, and twin boundaries to promote steady strain hardening, kink bands suppress these interactions as a strain-softening mechanism. These bands continually rotate the lattice to accommodate the exceptionally high strains near the crack tip, effectively distributing the damage.

Still, the observation of marked toughening in the presence of this strain softening mechanism was surprising. In the model for ductile fracture, the fracture toughness, J_{Ic} , is directly proportional to the flow stress (σ_f), strain to failure (ε_f), and a characteristic dimension

related to the spacing involved in microvoid coalescence ahead of a crack tip (l_0^*) , i.e., $J_{Ic} \approx \sigma_f \tilde{\varepsilon}_f l_0^*$ (45, 46). Whereas the exceptionally high fracture toughness of CrCoNi-based fcc HEAs results from the activation of multiple strain-hardening mechanisms that prolong uniform ductility and elevate flow stress (47, 48), something different is happening in Nb₄₅Ta₂₅Ti₁₅Hf₁₅. Softening from kink bands negatively impacts the flow stress (at room temperature, the alloy yields at 596 MPa and has an ultimate tensile strength of 640 MPa) as well as the uniform ductility. However, kink bands activate two other mechanisms that compensate for these drawbacks: (i) They prolong necking, which can substantially increase the fracture strain, as is evident in the tensile curves (Fig. 2C). This observation has been reported not only in RHEAs, but also in high-strength bcc Ti-alloys (49). (ii) The kink bands also increase the characteristic distance between the voids ahead of the crack tip. Our estimates of the characteristic spacing for void coalescence show that they must be ~242 μm apart to account for the exceptionally high minimum J_{Ic} values (474 kJ/m²). This value is a very large number, considering that void coalescence occurs on the order of 1 to 10 µm in CrCoNi at 20 K, where this material is toughest (19), We readily observed these microvoids on the fracture surface (Fig. 3K). Although they had a bimodal distribution due to the presence of small partially recrystallized grains, larger microvoids of an average size of \sim 140 \pm 52 μ m were apparent. Thus, when kink bands nucleate from regions of extremely high dislocation density to alleviate and distribute damage (26), they eliminate sites inside grains that lead to microvoid nucleation by providing a secondary, energetically favorable pathway for dislocations to form a low-angle grain boundary, which leads to high toughness.

Understanding the conditions that promote kink band formation is critical to the design of future RHEAs that circumvent the strengthtoughness trade-off. To this end, we identified two conditions in this alloy that we believe are essential for kink band formation by multiple slip systems. The first condition is an edge dislocation's "Goldilocks mobility." It has been postulated that kink bands occur by a depletion of slip systems required to maintain uniform plastic deformation (23–25). This describes kinking in hexagonal close-packed materials such as in zinc and cadmium, in which the basal slip system is energetically preferred (22, 25, 50, 51); however, this argument is inapplicable for bcc materials with 48 slip systems, necessitating a different perspective. Kink band formation in bcc materials must be enabled by another factor, which can be deduced to be the high edge dislocation velocities that are intrinsic to this crystal structure. High mobilities allow edge dislocations to interact on much shorter timescales at quasistatic strain rates. However, if they are too mobile, a potential high-temperature strengthening mechanism is lost (16). Our observation of edge and mixed dislocations suggests that they have relatively reduced mobilities, which could contribute to high-temperature strength, though this does not necessarily discount pinning of screw dislocations by atomic jogs as a hightemperature strengthening mechanism (17).

The second condition that is associated with kink band formation by multiple slip systems is an energetic isotropy of slip systems. In pure niobium, kink bands form by the <111>{110} slip systems (27, 52, 53), and alloying with group IV elements triggers a transition to additional kink band formation by the <111>{112} slip system, as seen in this work for Nb₄₅Ta₂₅Ti₁₅Hf₁₅. To understand this phenomenon, we calculated the generalized stacking fault energies (GSFEs) of the three possible slip systems $a_0/2<111>\{110\}, \{112\}, \text{ and } \{123\}$ —and compared them to pure Nb. We show the results in fig. S12, A to C, and summarize them in table S5. Whereas in pure Nb, the unstable stackingfault energy (USF) energy (the maximum on the GSFE profile) along {110} was 15% lower than that along {112} and {123}, this difference was reduced in Nb₄₅Ta₂₅Ti₁₅Hf₁₅, where the USF energies were equivalent in all three slip systems within the calculated statistical uncertainties. This energetic equivalence is absent in other pure refractory bcc metals and binary group V and VI alloys in which not only are GSFEs higher, but the <111>{110} slip system is energetically favored over that of {112} and {123} (54, 55). This suggests that edge dislocations on the <111>{112} system can be just as easily energetically accessed as those on <111>{112} in Nb₄₅Ta₂₅Ti₁₅Hf₁₅, which promotes glide and thus kink band formation by this system. These results do not consider the effects of short-range order. Although the low mixing energies of Nb, Ta, Ti, and Hf in this alloy suggest that it would have a low tendency to order, implying that this would have a minimal impact on GSFEs (28), the presence of short-range order can alter stacking fault energy, as is the case in the CrCoNi alloy (56). The addition of group IV elements (in this case, Ti and Hf) is essential to the formation of kink bands because these elements promote slip on <111>{112}.

Conclusions

Our work shows that contrary to conventional understanding, complex concentrated refractory alloys can possess exceptional fracture toughness across extreme temperature ranges, even in the cryogenic regime. Although further development is needed to increase the NbTaTiHf alloy's strength and grain boundary cohesion, its exceptional damage tolerance opens a door for use of these refractory alloys in safetycritical applications. To put the findings of our work in context, we compared its fracture toughness and strength to current commercial alloys (Fig. 5), highlighting the exceptional combination of high-temperature strength and very high toughness displayed by Nb₄₅Ta₂₅Ti₁₅Hf₁₅. Understanding kink band formation from first principles is essential to discovering more damage-tolerant RHEAs with high-temperature strength. The analysis that we present is a starting point with general guidelines related to dislocation mobility, activation of multiple slip systems, and formation of kink bands.

REFERENCES AND NOTES

- 1. R. O. Ritchie, Nat. Mater. 10, 817-822 (2011).
- J. H. Perepezko, Science 326, 1068–1069 (2009).
- 3. K. S. Chan, J. Miner. Met. Mater. Soc. 44, 30-38 (1992).
- 4. Y. Zou et al., Scr. Mater. 128, 95-99 (2017).
- J. A. Lemberg, R. O. Ritchie, Adv. Mater. 24, 3445–3480 (2012).
 D. B. Miracle, O. N. Senkov, Acta Mater. 122, 448–511 (2017).
- 7. O. N. Senkov, D. B. Miracle, K. J. Chaput, J.-P. Couzinie,
- J. Mater. Res. 33, 3092–3128 (2018).
 O. N. Senkov, G. B. Wilks, J. M. Scott, D. B. Miracle, Intermetallics 19, 698–706 (2011).
- 9. P. Kumar et al., Acta Mater. 245, 118620 (2023).
- X. J. Fan, R. T. Qu, Z. F. Zhang, J. Mater. Sci. Technol. 123, 70–77 (2022).
- 11. T. Li et al., Acta Mater. 246, 118728 (2023)
- 12. S. Y. Chen et al., Scr. Mater. 158, 50-56 (2019).
- 13. O. N. Senkov et al., J. Mater. Sci. 47, 4062-4074 (2012).
- 14. L. H. Mills et al., Acta Mater. 245, 118618 (2023).
- 15. F. Maresca, W. A. Curtin, Acta Mater. 182, 235-249 (2020).
- F. Wang et al., Science 370, 95–101 (2020).
 S. I. Rao, C. Woodward, B. Akdim, O. N. Senkov, D. Miracle, Acta Mater. 209, 116758 (2021).
- 18. W. A. Curtin, S. I. Rao, C. Woodward, MRS Bull. 47, 151–157 (2022).
- 19. D. Liu et al., Science **378**, 978–983 (2022).
- 20. S. Wang et al., Acta Mater. 201, 517-527 (2020).
- 21. H. Chen et al., Crystals (Basel) 11, 81 (2021).
- 22. E. Orowan, *Nature* **149**, 643–644 (1942).
- P. E. J. Flewitt, A. G. Crocker, Philos. Mag.: A Journal of Theoretical Experimental and Applied Physics 34, 877–891 (1976).
- A. G. Crocker, J. S. Abell, Philos. Mag.: A Journal of Theoretical Experimental and Applied Physics 33, 305–310 (1976).
- J. B. Hess, C. S. Barrett, J. Miner. Met. Mater. Soc. 1, 599–606 (2017).
- K. Li, W. Chen, G. Yu, J. Zhang, J. Sun, J. Alloys Compd. 875, 159982 (2021).
- C. Y. Chan, C. N. Reid, B. J. Duggan, *Mater. Sci. Technol.* 18, 449–457 (2013).
- P. P. P. O. Borges, R. O. Ritchie, M. Asta, *Acta Mater.* 262, 119415 (2024).
- 29. C. Zhang et al., Scr. Mater. 188, 16-20 (2020).
- 30. Materials and methods are available as supplementary materials. 31. S. Hertelé, W. De Waele, R. Denys, *Int. J. Non-linear Mech.* 46,
- 51. S. Hertele, W. De Waele, R. Denys, Int. J. Non-linear Mech. 46 519–531 (2011).
- M. Faleschini, H. Kreuzer, D. Kiener, R. Pippan, J. Nucl. Mater. 367-370, 800–805 (2007).
- 33. W.-Y. Kim, H. Tanaka, M.-S. Kim, S. Hanada, *Mater. Sci. Eng. A* **346**, 65–74 (2003).
- Y. Murayama, S. Hanada, Sci. Technol. Adv. Mater. 3, 145–156 (2018).
- 35. S.-P. Wang, E. Ma, J. Xu, Intermetallics 103, 78–87 (2018).
- K. Ramachandran, Y. C. Jayakody, D. D. Jayaseelan, Int. J. Refract. Hard Met. 110, 106033 (2023).
- S. Wurster, B. Gludovatz, R. Pippan, *Int. J. Refract. Hard Met.* 28, 692–697 (2010).
 R. Gröger, J. Holzer, T. Kruml, *Comput. Mater. Sci.* 216, 111874
- 39. M. Wu et al., J. Mater. Sci. Technol. **110**, 210–215 (2022).
- 40. S. Wang, M. Wu, D. Shu, B. Sun, *Mater. Lett.* **264**, 127369 (2020).
- 41. S. Zherebtsov et al., Adv. Eng. Mater. 22, 2000105 (2020).
- 42. T. Cao et al., J. Alloys Compd. 891, 161859 (2022).
- M. Yamasaki, K. Hagihara, S. Inoue, J. P. Hadorn, Y. Kawamura, *Acta Mater.* 61, 2065–2076 (2013).
- 44. W. T. Read, W. Shockley, Phys. Rev. 78, 275-289 (1950).
- 45. C. Lee et al., Nat. Commun. 12, 5474 (2021).
- A. C. Mackenzie, J. W. Hancock, D. K. Brown, *Eng. Fract. Mech.* 9, 167–188 (1977).
- R. O. Ritchie, A. W. Thompson, Metall. Trans., A, Phys. Metall. Mater. Sci. 16, 233–248 (1985).
- 48. B. Gludovatz et al., Science 345, 1153-1158 (2014).
- S. Sadeghpour, S. M. Abbasi, M. Morakabati, L. P. Karjalainen, J. Alloys Compd. 808, 151741 (2019).
- 50. K. C. A. Blasdale, R. King, Phys. Status Solidi B 10, 175-184 (1965).
- K. C. A. Blasdale, R. King, K. E. Puttick, *Phys. Status Solidi B* 18, 491–503 (1966).
- J. Nagakawa, M. Meshii, Philos. Mag. A Phys. Condens. Matter Defects Mech. Prop. 44, 1165–1191 (2006).

- 53. G. Taylor, J. W. Christian, *Philos. Mag.: A Journal of Theoretical Experimental and Applied Physics* **15**, 873–892 (1967).
- J. Qian, C. Y. Wu, J. L. Fan, H. R. Gong, J. Alloys Compd. 737, 372–376 (2018).
- N. I. Medvedeva, Y. N. Gornostyrev, A. J. Freeman, *Phys. Rev. Lett.* **94**, 136402 (2005).
- J. Ding, Q. Yu, M. Asta, R. O. Ritchie, *Proc. Natl. Acad. Sci. U.S.A.* 115, 8919–8924 (2018).
- Appendix A Data for Engineering Materials, Materials Selection in Mechanical Design, M. F. Ashby, Ed. (Butterworth-Heinemann, ed. 4, 2011), pp. 495–523.
- 58. Y. H. Jo et al., J. Alloys Compd. 844, 156090 (2020).
- 59. F. Chen et al., Mater. Des. 185, 108251 (2020).
- 60. P. Hu et al., J. Alloys Compd. 711, 64-70 (2017).
- A. Sengupta et al., J. Mater. Eng. Perform. 3, 73–81 (1994).
- Haynes International, Haynes Waspaloy alloy (2017); https://www.haynesintl.com/wp-content/uploads/2023/06/ waspaloy.pdf.
- Special Metals, Inconel alloy 625 (2013), pp. 1–18; https://www.specialmetals.com/documents/technical-bulletins/inconel/inconel-alloy-625.pdf.

ACKNOWLEDGMENTS

We appreciate the assistance of N. C. Levkulich, J. O. Brown, and L. Semiatin, Materials Resources LLC, in performing rolling trials in the metals processing facility of the Air Force Research Laboratory's Material and Manufacturing Directorate. We also thank M. Gronley from the machine shop at LBNL for his help and assistance. Funding: This research was primarily supported by the Materials Sciences and Engineering division of the US Department of Energy, Office of Science, Office of Basic Energy Sciences through the Damage-Tolerance in Structural Materials program (KC13) at the Lawrence Berkeley National Laboratory (LBNL) under contract DE-AC02-CH11231. Microscopy facilities were provided by the National Center for Electron Microscopy in the Molecular Foundry at LBNL, which is supported by the US Department of Energy Office of Science, Office of Basic Energy Sciences under contract DE-AC02-05CH11231, Atomistic simulations used resources from the National Energy Research Scientific Computing Center (NERSC), which is also supported by the Office of Basic Energy Sciences of the US Department of Energy under the same contract number. C.H.B., E.J.L., and D.A. acknowledge the use of the processing facilities at the UC Irvine. which is partially supported by the National Science Foundation Materials Research Science and Engineering Center program through the UC Irvine Center for Complex Active Materials (DMR-2011967). D.H.C. acknowledges the support of an NSF Graduate Fellowship from the National Science Foundation (grant no. DGE 2146752), Z.L. and A.D. acknowledge support from the Materials Sciences and Engineering division of the U.S. Department of Energy, Office of Science, Office of Basic Energy Sciences as a part of the Early Career Research program FWP 76052 for the ator probe tomography analysis conducted in PNNL. Author contributions: R.O.R., D.H.C., and P.K. conceived the project; C.H.B. processed the alloys, supervised by E.J.L. and D.A.; mechanical testing was carried out by D.H.C. and P.K., supervised by R.O.R.; transmission electron microscopy (STEM, TEM, and 4D-STEM) was performed by M.I.P. and M.Z., supervised by A.M.M.; atomistic simulations were performed by P.B., W.W., and F.W., supervised by M.A.; D.H.C. wrote the first draft of the manuscript, aided by R.O.R. and P.K., with all authors participating in the revision of the final paper; and R.O.R. supervised the entire project. **Competing interests:** The authors declare no competing interests. Data and materials availability: All data that support the findings of this study are reported in the main paper and supplementary materials. License information: Copyright © 2024 the authors, some rights reserved; exclusive licensee American Association for the Advancement of Science. No claim to original US government works. https://www. science.org/about/science-licenses-journal-article-reuse

SUPPLEMENTARY MATERIALS

science.org/doi/10.1126/science.adn2428 Materials and Methods Figs. S1 to S17 Tables S1 to S5 References (64–84)

Submitted 29 November 2023; accepted 6 March 2024 10.1126/science.adn2428